



LAWRENCE
LIVERMORE
NATIONAL
LABORATORY

Excitation Cross Section Measurement for $n=3$ to $n=2$ Line Emission in Fe^{17+} to Fe^{23+}

H. Chen, M. F. Gu, P. Beiersdorfer, K. R. Boyce, G. V. Brown, S. M. Kahn, R. L. Kelley, C. A. Kilbourne, F. S. Porter, J. H. Scofield

February 9, 2006

Astrophysical Journal

Disclaimer

This document was prepared as an account of work sponsored by an agency of the United States Government. Neither the United States Government nor the University of California nor any of their employees, makes any warranty, express or implied, or assumes any legal liability or responsibility for the accuracy, completeness, or usefulness of any information, apparatus, product, or process disclosed, or represents that its use would not infringe privately owned rights. Reference herein to any specific commercial product, process, or service by trade name, trademark, manufacturer, or otherwise, does not necessarily constitute or imply its endorsement, recommendation, or favoring by the United States Government or the University of California. The views and opinions of authors expressed herein do not necessarily state or reflect those of the United States Government or the University of California, and shall not be used for advertising or product endorsement purposes.

Excitation Cross Section Measurement for $n=3$ to $n=2$ Line Emission in Fe^{17+} to Fe^{23+}

H. Chen^{*}, M. F. Gu[†], P. Beiersdorfer^{*}, K.R. Boyce[§], G.V. Brown^{*}, S. M. Kahn[†], R. L. Kelley[§], C. A. Kilbourne[§], F. S. Porter[§] and J. H. Scofield^{*}

^{*} *High Temperature and Astrophysics Division, Lawrence Livermore National Laboratory,
Livermore, CA 94551*

[†] *Physics Department, Stanford University, CA 94305*

[§] *Goddard Space Flight Center, Greenbelt, MD 20771*

ABSTRACT

We report the measurement of electron impact excitation cross sections for the strong iron L-shell $3 \rightarrow 2$ lines of Fe XVIII through Fe XXIV at the EBIT-I electron beam ion trap using a crystal spectrometer and a 6×6 pixel array microcalorimeter. The cross sections were determined by direct normalization to the well established cross section of radiative electron capture through a sophisticated model analysis which results in the excitation cross section for 48 lines at multiple electron energies. We also studied the electron density dependent nature of the emission lines, which is demonstrated by the effective excitation cross section of the $3d \rightarrow 2p$ transition in Fe XXI.

Subject headings: atomic data—line: atomic processes: methods—X-rays: general

1. Introduction

Accurate atomic data are important for the modeling of observed line intensities and for deriving the plasma conditions which are critical in the interpretation of astrophysical observations (Kahn et al. 1990; Paerels & Kahn 2003). Particularly, the atomic data of iron are crucial for interpreting virtually all types of observations since iron is the most abundant high-Z element and radiates profusely in many spectral bands. Specifically, the spectral-rich emission from the iron L-shell has been one of the primary diagnostic tools of the high-resolution grating spectrometers on the *XMM – Newton* and *Chandra* X-ray observatories. Observations with these spacecraft are able to resolve many individual spectral features unresolved previously, and they allow for better plasma diagnostics based on these lines. A great deal of theoretical modeling effort has been put forward to interpret these high-resolution X-ray spectra. For example, Smith et al. (2001) presented an improved collisional-radiative plasma code APEC that has been widely used in astrophysical data analysis. Also, Behar, Cottam & Kahn (2001) have successfully used the HULLAC

atomic code (Bar-Shalom et al. 2001) to model Capella data obtained using the high-energy transmission grating of *Chandra*. Despite these efforts in improving the atomic calculations, the need for laboratory measurements is clear: repeatedly, laboratory data have shown that calculations are inaccurate or incomplete because they miss crucial physics left out as part of necessary approximations (Beiersdorfer 2003). A prime example is the significant discrepancy found between observations and code predictions, including those from APEC and HULLAC, in the analysis of Fe XVII and Fe XVIII line ratios (Behar, Cottam & Kahn 2001; Xu et al. 2002). Recent laboratory measurements show that these discrepancies, at least in the case of Fe XVII, are likely due to the accuracy of the excitation cross section of the resonance line (Beiersdorfer et al. 2004; Brown et al. 2006) .

To address the need for validating the calculations using experimental data, our laboratory X-ray astrophysics program, utilizing the electron beam ion traps EBIT-I and EBIT-II at the University of California Lawrence Livermore National Laboratory, has produced large sets of reliable atomic data, including ionization and recombination cross sections for charge balance calculations, emission line lists, excitation cross sections, and dielectronic recombination resonance strengths for interpreting X-ray line formation. An overview of this program was given by Beiersdorfer (2003). For iron, we have recently measured (within a lower limit intensity cutoff) a complete set of Fe L-shell emission line wavelengths (Brown et al. 2002, 1998). Various issues associated with the Fe XVII spectrum have been addressed and resolved, including presumed opacity effects, line blending, and cross section measurements (Brown et al. 1998, 2001, 2002, 2006; Beiersdorfer et al. 2002, 2004). Moreover, Gu et al. (1999a, 2001) have reported a set of iron L-shell excitation cross sections for the L-shell lines of Fe XXI–Fe XXIV that were normalized to calculations in the high energy limit. Although such a normalization can be fairly reliable at high electron-ion collision energies, the accuracy of electron scattering calculations is limited to 15 – 30% (Zhang et al. 1989), and may be much worse (factors of two or more, see Section 4 of this paper), if the levels are affected by configuration interactions. A more accurate method is normalizing directly to radiative electron capture, i.e. radiative recombination (RR). This is because RR, the inverse of photoionization, is the simplest atomic scattering process, which at high energy involves only one electron and one photon. An RR X-ray is produced by capturing a free electron into a bound level. The emitted photon has an energy equal to the sum of the free electron energy and the ionization potential of the level into which the electron is captured. At high electron energies, the RR cross sections are known both from calculations and from synchrotron measurements to an accuracy of 3–5% (Saloman et al. 1988).

Previously, measurements of some Fe L-shell cross sections utilizing RR for normalization were reported by Chen et al. (2002, 2005) and Brown et al. (2006). These measurements were made possible in part by the availability of a high-resolution, large-area, gain-stabilized microcalorimeter, the engineering spare microcalorimeter from the original *ASTRO – E* satellite mission. This instrument has unique characteristics that make such measurements possible, including the ability to time tag each X-ray event and an extended duty cycle. The measurements of Chen et al. (2002)

of three $n=3 \rightarrow 2$ emission lines in Fe XXIV represent the first use of a calorimeter for cross section measurements. Subsequent measurements focused on $n=3 \rightarrow 2$ emission lines from the charge states from Fe²⁰⁺ to Fe²³⁺ (Chen et al. 2005) and Fe¹⁶⁺ (Brown et al. 2006). The present work extends the electron excitation cross section measurements to the remaining strong $n=3 \rightarrow 2$ L-shell Fe lines. We report experimental cross sections for a total of 48 lines from Fe¹⁷⁺ to Fe²³⁺.

2. Experiments

Our experiments were carried out on the EBIT-I device (Levine et al. 1988). Similar to the experimental setup described in our previous measurement on EBIT-II (Chen et al. 2005), we used a crystal spectrometer (Beiersdorfer & Wargelin 1994; Brown et al. 1999) together with the XRS/EBIT microcalorimeter detector (Kelley et al. 1999; Stahle et al. 1999; Porter et al. 1999; Audley et al. 1999; Gendreau et al. 1999; Boyce et al. 1999). The microcalorimeter had an energy resolution better than 10 eV and a dynamic range from 0.1 to 10 keV. The crystal spectrometer employed a flat Rubidium hydrogen phthalate (RAP) crystal, which has an energy coverage of about 150 eV per setting. To cover the L-shell Fe lines from different charge states (photon energies between 0.78 to 1.18 keV, equivalent to wavelengths between 10.5 and 15.9 Å), we set the Bragg angles to 30.5, 32, 36 and 40 degrees for various electron beam energies from 1.35 to 2.93 keV. The crystal spectrometer had a resolving power of 385 (FWHM of 2.6 eV at a photon energy of 1 keV). Most of the strong Fe $3 \rightarrow 2$ L-shell lines observed with the crystal spectrometer were resolved, while only a few of those observed with the microcalorimeter were, illustrating the need to operate both instruments simultaneously. The L-shell Fe lines were previously measured by Brown et al. (2002) and their labels and identifications are used in this paper. Figure 1 shows a typical measurement at an electron energy of 1.35 keV from both the crystal spectrometer and the XRS. Strong lines, mostly from Ne-like and F-like ions, are marked.

The 6×6 XRS pixel array (30 were active during these measurements) of $625 \times 625 \mu\text{m}^2$ per pixel has unique features that enabled the present measurements. These are a combination of high effective area (10 mm^2), electronic stability, and a microsecond time resolution, and so far none of which has been duplicated in other calorimeter devices. This combination is needed because the RR cross sections are about two orders of magnitude smaller than the electron-impact excitation cross sections. In other words, only one RR X-ray is counted for 100 counts in a particular L-shell emission line. Thus, for these measurements, the XRS/EBIT microcalorimeter instrument must have a large dynamic range and be capable of long observations without significant gain drift.

The spectral response of the XRS has been photometrically calibrated between 300 eV and 10 keV (Audley et al. 1999) and was monitored during the experiments by recording the signal from an x-ray tube attached to the opposite view port. The response function of the XRS is given by the foil transmission and detector quantum efficiency. The 5 thin-foil filters are four Al/polyimide filters (each with thickness 545 Å/795 Å, 1023 Å/1045 Å, 1023 Å/1085 Å, and 1023 Å/1085 Å, respectively) and one Al/Parylene filter (200 Å/1000 Å) used to separate the XRS and EBIT-I

vacua as well as to reduce the thermal load on the XRS. Also, during the experiment we checked the filter response through measurement of the line ratios of O, N, and C to look for ice buildup and thus to account for any changes.

The efficiency of the crystal spectrometer was determined (using tabulated X-ray absorption cross sections) by taking into account the photon absorption of the window foils, including a $0.5\ \mu\text{m}$ polyimide window on the spectrometer, and a $1\ \mu\text{m}$ polyimide window on the position sensitive gas proportional counter. Also taken into account was the photon absorption of the P-10 (10% CH₄ and 90% Ar) gas that filled the proportional counter at 1 atmosphere pressure with a depth of 0.9 cm.

Iron was continuously injected into the trap as iron pentacarbonyl using a ballistic gas injector. This injection method has the advantage that the trap is fully filled with iron ions, leaving no space for ions of lower-Z elements such as oxygen (Brown et al. 2002). The ions were ionized by the beam and trapped for about 3 – 4 seconds. Then the trap was emptied and filled anew. Our measurements were made at electron beam energies of 1.35, 1.46, 1.56, 1.7, 1.82, 1.94, 2.05, 2.45, and 2.93 keV, with beam currents ranging between 20 – 30 mA. These energies were slightly above the ionization threshold of individual ion charge states from F-like to Li-like, and they were high enough so that the contributions from dielectronic recombination radiation and resonance excitation to the direct excitation line intensities can be ignored. At these energies, however, cascades from higher levels may contribute to the line intensities. Our method determines the effective cross section that includes all possible cascade processes at the given electron energies.

3. Data Analysis

As shown in Brown et al. (2002) the structure of Fe L-shell spectrum is very complex. The complexity was enhanced in our measurement because the iron was continuously introduced into the EBIT-I trap and step-wise ionized. This provides a continuous influx of low charge state ions. As a result, the charge balance inside the trap featured many lower charge states despite the fact that the electron beam energy was far greater than their ionization threshold. This is clearly illustrated by the presence of lines in the spectrum from lower charge states. Figure 2 shows a crystal spectrum taken at an electron energy of $E_b = 2.93\ \text{keV}$, on which we see the lines from low charge states such as C-like Fe XXI, and even Ne-like Fe XVII. A direct illustration of this fact also comes from the measured radiative recombination spectrum obtained with the XRS (Figure 3), where the radiative recombination to the fine structures of each levels can be seen as distinct peaks. The spectrum shows that all charge states between Fe XVIII and Fe XXIV are present in the trap. The presence of Fe XVII cannot be inferred from the L-shell RR because it has a closed L-shell.

To analyze these complicated spectra, we developed a new method based on the atomic data calculated with the Flexible Atomic Code (Gu 2003). The model starts with a theoretical data

base that includes thousands of lines, most of which were too weak to be measured experimentally but will contribute to the spectrum collectively. When comparing the theoretical model with the experimental data, we adjust the theoretical cross sections for a subset of strong lines in order to achieve acceptable agreement. This allows us to derive the measured cross sections for this subset of lines, and any possible contamination of weak lines in the determination of intensities of strong lines are accounted for in the analysis with theoretical calculations. In the following we describe the principles of this method, using the spectrum taken at $E_b = 2.93$ keV as an example.

The basic model for fitting both the crystal and calorimeter spectra is constructed as

$$I(x) = \sum_i A_{q_i} \eta_i \sigma_i G_i \phi(x - x_i) + b(x), \quad (1)$$

where $I(x)$ is the photon counts at channel x , $b(x)$ is the background model usually taken as a constant or a linear function of x , x_i is the spectral channel corresponding to the energy or wavelength (λ_i) of line i , σ_i is the line formation cross section, η_i is the spectrometer efficiency, $\phi(x - x_i)$ represents the line profile, and A_{q_i} is the relative abundance of the ion which produces line i . All wavelength and charge state independent constant factors such as the electron density, velocity, collection solid angle of the detector, etc, are also absorbed in the A_q parameters. G_i is the polarization and anisotropy correction factor for line i . For the XRS, only the anisotropy factor W_i is relevant, and for E1 transitions, it is related to the polarization of the line as

$$G_i = W_i = \frac{3}{3 - P_i}. \quad (2)$$

For the crystal spectrometer, an additional factor due to the crystal reflectivity difference in the two polarization components is present, and

$$G_i = \left(1 + \frac{1 - f_i}{1 + f_i} P_i \right) W_i, \quad (3)$$

where $f_i = R_\pi/R_\sigma$, and R_π (R_σ) is the crystal reflectivity for radiation polarized parallel (perpendicular) to the dispersion plane.

At each experimental beam energy, the theoretical values of G_i , σ_i , and λ_i for all significant emission lines from $L - shell$ Fe ions are calculated with the Flexible Atomic Code (Gu 2003). In these calculations, only direct excitation and cascade contributions from levels up to $n = 7$ are included. For $3 \rightarrow 2$ transition wavelengths, the accurate many-body perturbation theory results of Gu (2005) are used, which are shown to be better than a few mÅ in comparison with the experimental results of Brown et al. (2002). The theoretical values of $I_{rr} = G_i \sigma_i$ for the RR emission lines onto $n = 2$ subshells were calculated with a Dirac Hartree-Fock model and tabulated in Chen et al. (2005).

The experimental cross sections for a subset of the $3 \rightarrow 2$ emission lines are determined in the following procedure relative to the theoretical results for RR emission cross sections.

1. The XRS spectrum for the $n = 2$ RR emission is fitted, fixing all theoretical cross sections and relative positions of RR emission peaks. An overall shift of the RR spectrum is allowed to account for the uncertainty in the beam energy. The fit produces A_q parameters for all significant charge states present in the trap, which we denote as A_q^{RR} . The resulting charge balance for the $E_b = 2.93$ keV measurement from this step is shown in Fig. 4 (top).
2. Some charge states have very small concentrations, and their abundances cannot be determined with the RR emission given the poor counting statistics associated with these charge states (cf. Fig.3). However, due to the much larger cross sections for $3 \rightarrow 2$ emission lines, they may still contribute to the line spectrum in both crystal and the XRS spectrometers, and affect the determination of intensities of nearby lines. Utilizing the broadband nature of the XRS spectrometer, we fit the $3 \rightarrow 2$ line spectrum in XRS, fixing all theoretical excitation cross sections, G_i factors, and derive an estimate for the A_q parameters denoted as A_q^X . The resulting charge balance measurement from this step is shown in Fig. 4 (middle) for $E_b = 2.93$ keV. A_q^X values generally agree well with A_q^{RR} derived in the previous step, except for ions with small concentrations, where the statistical uncertainties in the A_q^{RR} values are substantial due to the small number of counts in the RR emission peak. Due to the limited spectral resolution of the XRS detector, the majority of the $3 \rightarrow 2$ emission lines are not resolved. The good agreement between the A_q^X and A_q^{RR} values derived in the previous two steps is an indication of the overall good quality of the theoretical excitation cross sections for strong $3 \rightarrow 2$ transitions. In order to obtain cross sections for individual lines, we take advantage of the high resolution of crystal spectrometers in the following steps.
3. The crystal spectrum of $3 \rightarrow 2$ lines is fitted, fixing all theoretical cross sections and G_i factors. In this step, the relative values of A_q factors are also fixed according to A_q^X values, and only the overall normalization factor is allowed to vary. The resulting A_q parameters are denoted as A_q^C , which is actually the same as A_q^X up to a constant factor. The purpose of this step is to determine the overall normalization difference between the crystal and XRS spectrometers.
4. The same crystal spectrum is fitted again, fixing the A_q^C parameters as derived in the previous step, but varying the cross sections of a subset of $3 \rightarrow 2$ lines, for which the experimental determination is desired. This subset of lines includes all strong and relatively unblended transitions present in the spectrum. The result of this step is a set of experimentally determined cross sections σ_i^C with a normalization determined according to the previous steps. The fit is shown in Fig. 2 for $E_b = 2.93$ keV. The purpose of this step is to determine the relative line cross sections within a single charge state.
5. With the line cross sections fixed as derived in the previous step, we fit the XRS spectrum of $3 \rightarrow 2$ lines again, and derive a different set of A_q parameters denoted as A_q^{XC} . Because the

$3 \rightarrow 2$ cross sections used in this step incorporate the information obtained with the crystal spectrometers, it effectively fixes the ratio of line excitation cross sections of the same charge state according to the crystal spectrum. The resulting charge balance from this step is shown in Fig. 4 (bottom), and the fit to the XRS spectrum is shown in Fig. 5 for the $E_b = 2.93$ keV measurement.

6. The cross sections, σ_i^C , derived in the fourth step is only relative in the sense that they give the correct ratios within the same charge state according to the crystal spectrum. The final experimental cross sections, σ_i^{XC} , relative to the RR emission are determined by comparing A_q^{XC} and A_q^{RR} , i.e.,

$$\sigma_i^{XC} = \frac{A_{qi}^{XC}}{A_{qi}^{RR}} \sigma_i^C. \quad (4)$$

The essential feature of this multi-step process is that the line cross section ratios within the same charge state are derived from the high-resolution crystal spectrometer, while the overall normalization for each charge state is derived from the comparison of $3 \rightarrow 2$ and RR emission in the XRS detector.

In the fit to the RR emission, the line profile is assumed to be a Gaussian function, whose width is dominated by the beam energy spread, and is left as a free parameter. When fitting the collisional excitation emission, the line profiles in both crystal spectrometer and XRS are set to be Voigt functions. The width and damping parameters are also determined in the fitting. The conversion between X-ray energy and spectral channels for the XRS is calibrated in the beginning of the experiment using H-like and He-like lines of various elements covering the 0–10 keV range. The conversion between the wavelength and channels for the crystal spectrometer at each crystal setting is determined by choosing several strong Fe L-shell lines as the calibration lines.

The uncertainty of the resulting cross section is a quadrature summation of the uncertainties from (a) the counting statistics for individual lines in the crystal data, (b) the counting statistics for the RR peak, (c) the uncertainty due to polarization corrections, which is a linear interpolation between unpolarized (zero uncertainty) and fully polarized lines (10%), and (d) the uncertainty due to background modeling in both crystal and XRS spectra, estimated to be about 10%.

4. Results and discussion

The results from the experiments are listed in Tables 1 and 2 for different charge states at various electron energies. Also listed in the tables are the calculation results using FAC and the values from previous measurements described by Chen et al. (2005). The atomic transitions for the lines are listed in Table 3. We plotted the measured cross sections and theory calculations from the FAC and the the HULLAC code (Bar-Shalom et al. 2001) for a couple of representative lines in Figs. 6 – 12 for F-like, O-like, N-like, C-like B-like, Be-like, and Li-like ions, respectively. In these

figures we also plotted all available previous measurements for comparison.

Overall the calculations agree well (the differences are less than 20%) with the experimental results for all lines, except for a couple of F-like lines (F20a, F20b, F19a, and F17) at electron energies of 1.56 KeV and 1.7 keV where the difference between theory and measurements differ by 30% and greater. The cause of this discrepancy is not clear.

Comparing the present measurements with previous measurements, we note that, except for lines C10 and Be1, the agreements are very good for the rest of the lines. We investigated further and found that the cause for this disagreement may be the following.

For the C-like Fe line C10, the previous measurement (Chen et al. 2005) resulted in a cross section that was about half of the present measurement. We believe that the difference very likely reflects a physical property of this line. C10 is among several lines that are sensitive to the electron density due to the collisional changes in the population of the $n=2$ fine-structure levels (Wargelin et al. 1998; Decaux et al. 2003; Chen et al. 2004). We have thus calculated the effective excitation cross sections as a function of electron density for 6 lines from different charge states. The results are shown in Fig. 7. Note that the C10 is the most density sensitive line of all: the first and second excited levels of C-like Fe XXI, $1s^2 2s^2 2p^2$ $J=1$ and $J=2$, are significantly populated for $n_e > 1 \times 10^{12} \text{cm}^{-3}$. In fact, for $n_e = 5 \times 10^{12} \text{cm}^{-3}$, the fractional population of the ground state is only 0.53, which means the effective excitation cross section from the true ground state is about half of what it is at lower electron density ($n_e < 10^{11} \text{cm}^{-3}$). This density dependence is the likely explanation for the differences between our present measurement and the previous measurements of Chen et al. (2005). In the present measurement on EBIT-I we had electron beam currents of about 20-30 mA. The diameter of the beam is taken as $60 \mu\text{m}$ (Utter et al. 1999), if we assume a 30% of beam-ion overlap ratio, then the electron density is about $n_e = 5 \times 10^{11} \text{cm}^{-3}$. This value is consistent with our measurement of the electron density on EBIT-I using spectral line ratios (Chen et al. 2004). The measurement described in paper by Chen et al. (2005) was taken on EBIT-II, which may have had a tighter beam diameter namely $50 \mu\text{m}$ and a higher (50%) beam ion overlap. This, together with a higher beam current (60 mA), could have resulted in a factor of 5–7 higher electron density, which is about a $n_e = 3\text{--}5 \times 10^{12} \text{cm}^{-3}$.

The Be1 ($2p_{3/2} - 3s_{1/2}$) line is the other line that does not agree with the previous measurement. The previous measurement indicates a somewhat (about 15–20%) lower value. This resulted from the fact that the Be1 line (12.161 \AA) was treated as a blend with the B-like line B6 ($2p_{3/2,1/2} - 3d_{5/2}$). In doing so, Chen et al. (2005) relied on the database by Brown et al. (2002), where the B6 line was assigned a wavelength of 12.144 \AA . To account for the blend, a contribution of about 10–15% of total intensity was assigned to originate from B6. However, we now find that the wavelength of B6 is actually 12.125 \AA , which is well separated from Be1. Correcting for this erroneous line blending assumption results in about a 15% increase in the Be1 intensity bringing the cross section measurement into agreement with our measurement reported here, as shown in Fig. 11.

This work was performed under the auspices of the U.S. Department of Energy by the University of California Lawrence Livermore National Laboratory under contract No. W-7405-Eng-48 and supported by NASA Astronomy and Physics Research and Analysis grants to LLNL, GSFC, and Stanford University.

.

Table 1. Effective cross sections of Fe XVIII-XX lines in units of 10^{-21}cm^2 . For each transition, the upper entry represents the present measurement, and the numbers in the brackets are the combined uncertainties. The lower entry represents the theoretical cross section. The superscript denotes whether the line is blended with other significant lines. If the superscript is 0, then the line is well isolated from other strong lines, although it may have weak blends whose intensities are fixed at the theoretical values during the fitting. Lines having the same superscript and the same energy are blended lines, whose cross section ratios are fixed at the theoretical value in the fitting, therefore, their measured cross sections are not independent of each other. The wavelengths are from measurement Brown et al. (2002), marked with [1], and present theoretical calculation using FAC, marked with [2].

Label	Wavelength(Å)		Electron energies					
	[1]	[2]	1.35 keV	1.46 keV	1.56 keV	1.70 keV	1.82 keV	1.94 keV
F20a	14.208	14.203	36.6[5.4] 40.1 ¹	36.1[5.4] 39.4 ⁴	29.0[4.5] 38.7 ⁵	28.1[4.9] 37.7 ⁴	—	—
F20b	14.208	14.209	20.2[3.0] 22.1 ¹	19.8[3.0] 21.6 ⁴	15.9[2.4] 21.2 ⁵	15.3[2.6] 20.5 ⁴	—	—
F19a	14.256	14.257	9.8[1.5] 8.9 ²	9.5[1.4] 8.7 ⁵	6.6[1.0] 8.5 ⁶	5.8[1.0] 8.3 ⁵	—	—
F19b	14.256	14.258	4.2[0.6] 3.8 ²	3.9[0.6] 3.6 ⁵	— —	— —	—	—
F17	14.373	14.374	15.9[2.3] 15.5 ⁰	14.5[2.2] 15.1 ⁰	11.5[1.8] 14.8 ⁰	— —	—	—
F15	14.534	14.536	13.2[2.0] 12.8 ³	— —	— —	— —	—	—
F14	14.571	14.553	6.2[0.9] 6.1 ³	— —	— —	— —	—	—
F11	15.625	15.624	17.3[2.5] 16.6 ⁰	— —	— —	— —	—	—
O26a	13.462	13.462	— —	3.8[0.6] 3.8 ²	3.7[0.6] 3.8 ³	3.7[0.6] 3.7 ²	—	—
O26b	13.462	13.464	— —	7.5[1.0] 7.5 ²	7.2[1.0] 7.4 ³	7.2[1.0] 7.1 ²	—	—
O25	13.497	13.506	— —	12.5[1.7] 13.1 ³	12.0[1.6] 12.8 ⁴	11.4[1.7] 12.5 ³	—	—
O24	13.518	13.521	— —	26.0[3.4] 27.3 ³	24.9[3.4] 26.8 ⁴	23.9[3.5] 26.0 ³	—	—
N33a	12.576	12.570	— —	— —	0.8[0.1] 1.0 ¹	— —	1.0[0.2] 1.0 ⁵	1.1[0.2] 1.0 ⁵
N33b	12.576	12.581	— —	— —	2.2[0.3] 2.8 ¹	— —	2.8[0.4] 2.8 ⁵	3.0[0.5] 2.7 ⁵
N33c	12.576	12.582	— —	— —	1.7[0.2] 2.1 ¹	— —	2.1[0.3] 2.1 ⁵	2.3[0.4] 2.1 ⁵
N31a	12.864	12.811	— —	8.0[1.3] 7.2 ¹	6.7[0.9] 7.0 ²	6.8[0.9] 6.8 ¹	6.5[1.0] 6.6 ⁶	6.4[1.0] 6.4 ⁶
N31b	12.846	12.826	— —	20.3[3.2] 18.2 ¹	17.1[2.2] 17.8 ²	17.4[2.3] 17.3 ¹	16.8[2.4] 16.9 ⁶	16.6[2.5] 16.5 ⁶
N31c	12.864	12.846	— —	17.5[2.8] 15.7 ¹	14.7[1.9] 15.4 ²	15.0[2.0] 14.8 ¹	14.4[2.1] 14.5 ⁶	14.1[2.1] 14.1 ⁶
N9	14.267	14.270	— —	— —	5.2[0.7] 6.6 ⁶	4.3[0.6] 6.2 ⁵	— —	—

Table 2. Effective cross sections of Fe XXI-XXIV lines in units of 10^{-21}cm^2 . The notation is the same as in Table 1. Three additional energy columns marked with \star list values from the earlier measurement of Chen et al. (2005)

Label	Wavelength(Å) [1]	[2]	1.70 keV	1.82 keV	1.94 keV	Electron energies 2.05 keV	\star 2.10 keV	2.45 keV	\star 2.50 keV	2.93 keV	\star 3.0 keV
C13	11.975	11.976	—	3.6[0.6] 3.0 ⁰	3.9[0.6] 3.0 ⁰	4.1[0.7] 3.0 ⁰	—	3.5[0.6] 2.9 ⁰	—	3.7[0.8] 2.9 ⁰	—
C11	12.044	12.201	—	1.4[0.2] 1.1 ³	—	—	—	—	—	—	—
C10	12.284	12.285	34.3[4.8] 36.5 ⁰	34.4[5.0] 35.7 ⁰	33.8[5.0] 34.9 ⁰	36.4[5.5] 34.3 ⁰	16.3[3.3] 32.3	32.2[5.2] 32.1 ⁰	—	32.2[6.3] 29.9 ⁰	11.5 ⁰ 29.9 ⁰
C8	12.393	12.398	—	8.3[1.2] 6.2 ⁰	7.6[1.1] 6.0 ⁰	7.3[1.1] 5.9 ⁰	4.3[0.9] 5.6	6.5[1.0] 5.6 ⁰	—	6.8[1.3] 5.2 ⁰	4.0 ⁰ 5.2 ⁰
C*	—	12.47	—	1.2[0.2] 0.9 ⁰	0.9[0.1] 0.8 ⁰	—	—	—	—	—	—
C6	12.499	12.497	—	0.8[0.1] 0.7 ⁴	—	—	—	—	—	—	—
C6	12.499	12.502	—	2.4[0.3] 2.1 ⁴	2.4[0.3] 1.9 ⁴	—	—	—	—	—	—
C*	—	12.597	—	0.7[0.1] 0.7 ⁵	0.8[0.1] 0.7 ⁵	—	—	—	—	—	—
C4	12.822	12.812	5.6[0.7] 5.5 ¹	5.4[0.7] 5.4 ⁶	5.3[0.7] 5.3 ⁶	—	5.7[1.0] 4.9	—	—	—	7.5 ⁰ 4.9
C3	13.521	13.503	7.9[1.0] 8.6 ³	—	—	—	—	—	—	—	—
B19	11.427	11.425	—	4.0[0.6] 3.3 ⁰	3.0[0.4] 3.3 ¹	3.5[0.5] 3.2 ¹	3.4[0.6] 3.2	3.2[0.5] 3.2 ²	2.6[0.6] 3.2	3.6[0.6] 3.1 ²	3.6 ⁰ 3.1 ²
B18a	11.490	11.481	—	2.1[0.3] 2.0 ¹	2.2[0.3] 2.0 ²	2.0[0.3] 2.0 ²	—	2.2[0.3] 2.0 ³	—	2.3[0.4] 2.0 ³	2.3 ⁰ 2.0 ³
B18b	11.490	11.493	—	1.2[0.2] 1.2 ¹	1.3[0.2] 1.2 ²	1.1[0.2] 1.2 ²	—	1.2[0.2] 1.1 ³	—	1.2[0.2] 1.0 ³	1.2[0.2] 1.0 ³
B13	11.770	11.77	—	18.6[2.5] 18.6 ⁰	17.7[2.4] 18.1 ⁰	16.6[2.2] 17.7 ⁰	15.9[2.5] 17.4	16.6[2.3] 16.4 ⁰	11.5[2.1] 16.2	16.8[2.7] 15.1 ⁰	13.5 ⁰ 15.1 ⁰
B10a	11.932	11.923	—	2.3[0.3] 2.4 ²	2.0[0.3] 2.1 ³	1.7[0.2] 1.9 ³	4.4[0.8] 5.2	1.2[0.2] 1.4 ⁴	—	0.9[0.2] 1.0 ⁴	4.2 ⁰ 1.0 ⁴
B10b	11.932	11.937	—	3.4[0.5] 3.6 ²	3.4[0.5] 3.5 ³	3.1[0.4] 3.4 ³	—	2.7[0.4] 3.2 ⁴	—	2.8[0.5] 2.9 ⁴	2.8 ⁰ 2.9 ⁴
B5	12.210	12.2	—	3.8[0.5] 3.1 ³	3.2[0.4] 3.0 ⁰	2.9[0.4] 2.9 ⁰	—	2.4[0.4] 2.7 ⁰	—	3.1[0.5] 2.4 ⁰	3.1 ⁰ 2.4 ⁰
B*	—	12.499	—	1.9[0.3] 1.6 ⁴	1.9[0.3] 1.5 ⁴	—	—	—	—	—	—
B4	12.754	12.752	—	6.6[0.9] 7.5 ⁰	6.4[0.8] 7.1 ⁰	—	—	—	—	—	—
Be9	10.981	10.981	—	—	5.3[0.8] 6.6 ⁰	5.6[0.8] 6.5 ⁰	6.4[0.6] 6.6	6.2[0.9] 6.5 ⁰	6.2[0.9] 6.6	6.3[1.0] 6.3 ⁰	6.3 ⁰ 6.3 ⁰
Be8	11.019	11.019	—	—	3.8[0.6] 4.2 ⁰	4.2[0.6] 4.2 ⁰	4.4[0.4] 4.3	3.9[0.6] 4.1 ¹	4.1[0.6] 4.1	4.2[0.7] 3.9 ¹	4.2 ⁰ 3.9 ¹
Be4	11.458	11.444	—	—	1.7[0.2] 1.8 ¹	1.7[0.2] 1.6 ¹	1.2[0.2] 1.6	1.0[0.1] 1.0 ²	0.8[0.2] 1	—	0.8 ⁰ 1
Be2	11.736	11.74	—	—	14.3[1.9] 16.1 ⁰	15.4[2.0] 15.8 ⁰	15.8[1.4] 15.7	15.3[2.0] 14.6 ⁰	11.4[1.6] 14.7	14.2[2.1] 13.4 ⁰	12.5 ⁰ 13.4 ⁰
Be1	12.161	12.159	—	—	7.8[1.0] 9.3 ⁰	7.7[1.0] 8.9 ⁰	6.4[0.6] 8.7	7.1[0.9] 7.7 ⁰	5.7[0.8] 7.6	6.4[1.0] 6.6 ⁰	5.3 ⁰ 6.6 ⁰
Li6	10.618	10.62	—	—	—	—	3.5[0.3] 4.5	4.2[0.6] 4.3 ⁰	4.1[0.5] 4.3	4.3[0.6] 4.0 ⁰	3.6 ⁰ 4.0 ⁰
Li5	10.663	10.663	—	—	—	—	1.8[0.2] 2.4	1.7[0.2] 2.2 ⁰	2.0[0.3] 2.3	1.8[0.3] 2.1 ⁰	2.1 ⁰ 2.1 ⁰
Li4	11.029	11.03	—	—	—	—	3.7[0.3] 3.6	3.0[0.4] 3.1 ¹	3.0[0.4] 3.1	3.0[0.4] 2.7 ¹	2.9 ⁰ 2.7 ¹
Li3	11.176	11.175	—	—	—	5.9[0.9] 6.4 ⁰	7.1[0.6] 5.6 ⁰	5.1[0.7] 5.6	5.2[0.6] 5.6	5.8[0.8] 4.9 ⁰	5.3 ⁰ 4.9 ⁰
Li1	11.432	11.43	—	—	—	—	3.4[0.3] 3.4	2.9[0.4] 2.9 ²	2.7[0.4] 2.9	2.9[0.4] 2.5 ²	2.3 ⁰ 2.5 ²

Table 3. Atomic Transitions associated with line labels used in the text.

Isoelectronic sequence	Label	Atomic Transition
9	F20a	$2p_{1/2}2p_{3/2}^33d_{3/2}(J=2-May) \rightarrow 2p_{3/2}^3(J=2-Mar)$
9	F20b	$2p_{1/2}2p_{3/2}^33d_{3/2}(J=2-Mar) \rightarrow 2p_{3/2}^3(J=2-Mar)$
9	F19a	$2p_{1/2}2p_{3/2}^33d_{3/2}(J=2-Jan) \rightarrow 2p_{3/2}^3(J=2-Mar)$
9	F19b	$2p_{1/2}2p_{3/2}^33d_{5/2}(J=2-May) \rightarrow 2p_{3/2}^3(J=2-Mar)$
9	F17	$2p_{1/2}2p_{3/2}^33d_{3/2}(J=2-May) \rightarrow 2p_{3/2}^3(J=2-Mar)$
9	F15	$2p_{3/2}^23d_{5/2}(J=2-May) \rightarrow 2p_{3/2}^3(J=2-Mar)$
9	F14	$2p_{3/2}^23d_{5/2}(J=2-Mar) \rightarrow 2p_{3/2}^3(J=2-Mar)$
9	F11	$2p_{1/2}2p_{3/2}^33s_{1/2}(J=2-May) \rightarrow 2p_{3/2}^3(J=2-Mar)$
8	O26a	$2p_{1/2}2p_{3/2}^23d_{3/2}(J=1) \rightarrow 2p_{3/2}^2(J=0)$
8	O26b	$2p_{1/2}2p_{3/2}^23d_{3/2}(J=1) \rightarrow 2p_{3/2}^2(J=2)$
8	O25	$2p_{1/2}2p_{3/2}^23d_{3/2}(J=2) \rightarrow 2p_{3/2}^2(J=2)$
8	O24	$2p_{1/2}2p_{3/2}^23d_{5/2}(J=3) \rightarrow 2p_{3/2}^2(J=2)$
7	N33a	$2s_{1/2}2p_{3/2}3p_{3/2}(J=2-Jan) \rightarrow 2p_{3/2}(J=2-Mar)$
7	N33b	$2s_{1/2}2p_{1/2}2p_{3/2}^23p_{3/2}(J=2-May) \rightarrow 2p_{3/2}(J=2-Mar)$
7	N33c	$2s_{1/2}2p_{3/2}3p_{3/2}(J=2-Mar) \rightarrow 2p_{3/2}(J=2-Mar)$
7	N31a	$2p_{1/2}2p_{3/2}3d_{3/2}(J=2-Jan) \rightarrow 2p_{3/2}(J=2-Mar)$
7	N31b	$2p_{1/2}2p_{3/2}3d_{3/2}(J=2-Mar) \rightarrow 2p_{3/2}(J=2-Mar)$
7	N31c	$2p_{1/2}2p_{3/2}3d_{5/2}(J=2-May) \rightarrow 2p_{3/2}(J=2-Mar)$
7	N9	$2s_{1/2}2p_{3/2}3s_{5/2}(J=2-Mar) \rightarrow 2s_{1/2}2p_{3/2}^2(J=2-May)$
6	C13	$2s_{3/2}3p_{3/2}(J=1) \rightarrow 2p_{1/2}^2(J=0)$
6	C11	$2s_{1/2}2p_{1/2}2p_{3/2}3d_{3/2}(J=2) \rightarrow 2s_{1/2}2p_{3/2}(J=1)$
6	C10	$2p_{1/2}3d_{3/2}(J=1) \rightarrow 2p_{1/2}^2(J=0)$
6	C8	$2p_{1/2}3d_{3/2}(J=1) \rightarrow 2p_{1/2}2p_{3/2}(J=1)$
6	C*	$2s_{1/2}3d_{5/2}(J=3) \rightarrow 2s_{1/2}2p_{3/2}(J=2)$
6	C6a	$2s_{1/2}3d_{3/2}(J=2) \rightarrow 2s_{1/2}2p_{3/2}(J=2)$
6	C6b	$2p_{1/2}3d_{5/2}(J=3) \rightarrow 2p_{1/2}2p_{3/2}(J=2)$
6	C*	$2p_{3/2}3d_{5/2}(J=1) \rightarrow 2p_{3/2}^2(J=0)$
6	C4	$2s_{1/2}3d_{5/2}(J=2) \rightarrow 2s_{1/2}2p_{3/2}(J=1)$
6	C3	$2s_{1/2}3s_{1/2}(J=0) \rightarrow 2s_{1/2}2p_{3/2}(J=1)$
5	B19	$2s_{1/2}2p_{1/2}3p_{3/2}(J=2-Mar) \rightarrow 2p_{1/2}(J=2-Jan)$
5	B18a	$2s_{1/2}2p_{1/2}3p_{3/2}(J=2-Jan) \rightarrow 2p_{1/2}(J=2-Jan)$
5	B18b	$2s_{1/2}2p_{1/2}3p_{3/2}(J=2-Mar) \rightarrow 2p_{1/2}(J=2-Jan)$
5	B13	$3d_{3/2}(J=2-Mar) \rightarrow 2p_{1/2}(J=2-Jan)$
5	B10a	$3d_{5/2}(J=2-May) \rightarrow 2p_{3/2}(J=2-Mar)$
5	B10b	$3d_{3/2}(J=2-Mar) \rightarrow 2p_{3/2}(J=2-Mar)$
5	B5	$2s_{1/2}2p_{1/2}3d_{5/2}(J=2-May) \rightarrow 2s_{1/2}2p_{1/2}2p_{3/2}(J=2-Mar)$
5	B*	$3s_{1/2}(J=2-Jan) \rightarrow 2p_{3/2}(J=2-Mar)$
5	B4	$2s_{1/2}2p_{1/2}3s_{1/2}(J=2-Jan) \rightarrow 2s_{1/2}2p_{1/2}2p_{3/2}(J=2-Mar)$
4	Be9	$2s_{1/2}3p_{3/2}(J=1) \rightarrow 2s_{1/2}^2(J=0)$
4	Be8	$2s_{1/2}3p_{1/2}(J=1) \rightarrow 2s_{1/2}^2(J=0)$
4	Be4	$2s_{1/2}3d_{5/2}(J=3) \rightarrow 2s_{1/2}2p_{3/2}(J=2)$
4	Be2	$2s_{1/2}3d_{5/2}(J=2) \rightarrow 2s_{1/2}2p_{3/2}(J=1)$
4	Be1	$2s_{1/2}3s_{1/2}(J=0) \rightarrow 2s_{1/2}2p_{3/2}(J=1)$
3	Li6	$3p_{3/2}(J=2-Mar) \rightarrow 2s_{1/2}(J=2-Jan)$
3	Li5	$3p_{1/2}(J=2-Jan) \rightarrow 2s_{1/2}(J=2-Jan)$
3	Li4	$3d_{3/2}(J=2-Mar) \rightarrow 2p_{1/2}(J=2-Jan)$
3	Li3	$3d_{5/2}(J=2-May) \rightarrow 2p_{3/2}(J=2-Mar)$
3	Li1	$3s_{1/2}(J=2-Jan) \rightarrow 2p_{3/2}(J=2-Mar)$

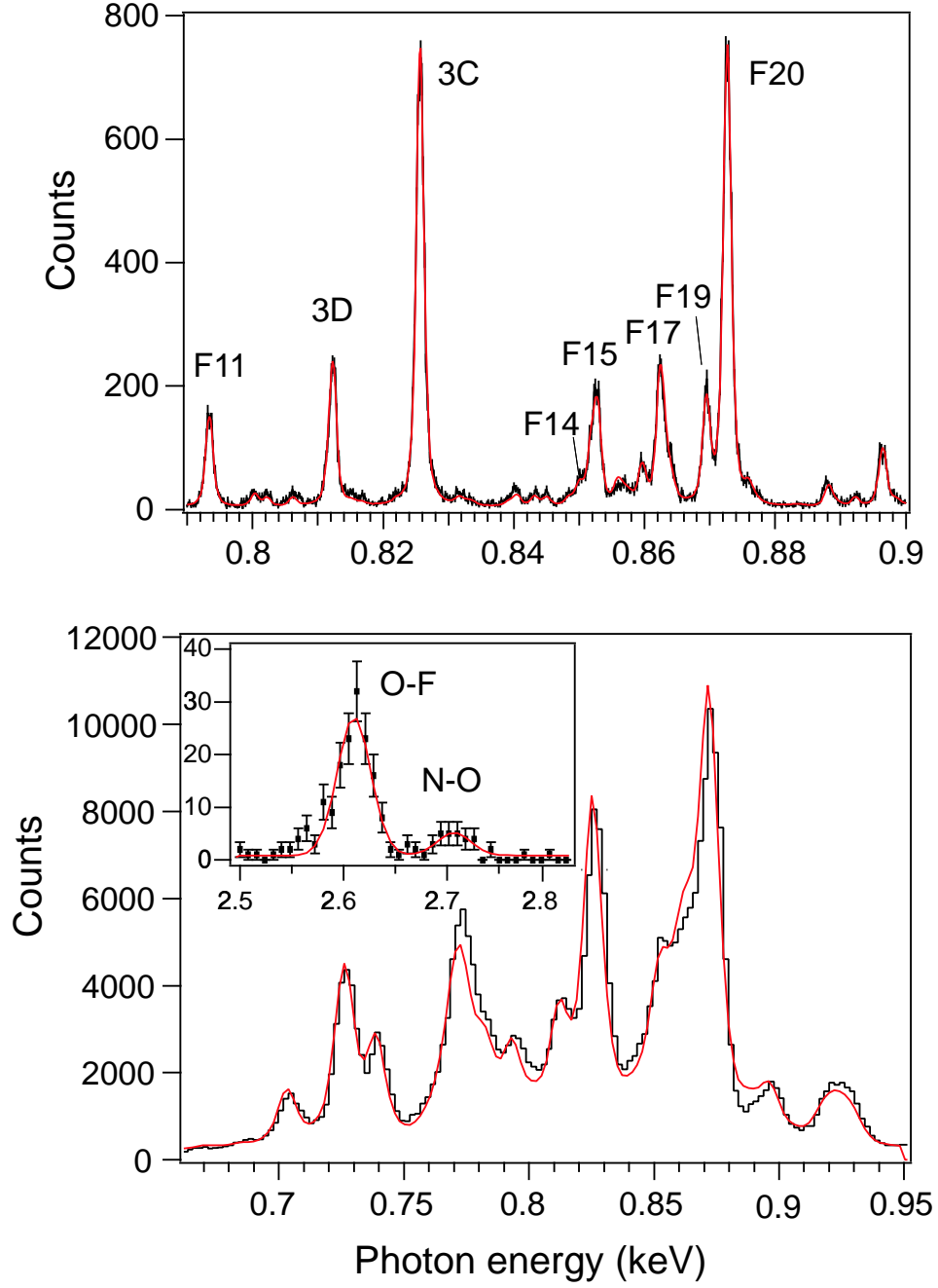


Figure 1. Fe spectra at an electron energy of 1.35 keV. The measured spectra are represented by a black line and the fitted ones by a red line. The top figure is the crystal spectrum, where strong lines are labeled. The bottom figure is a section ($3 \rightarrow 2$ transitions) from the XRS. The insert is the Fe L-shell radiative recombination spectrum from the XRS.

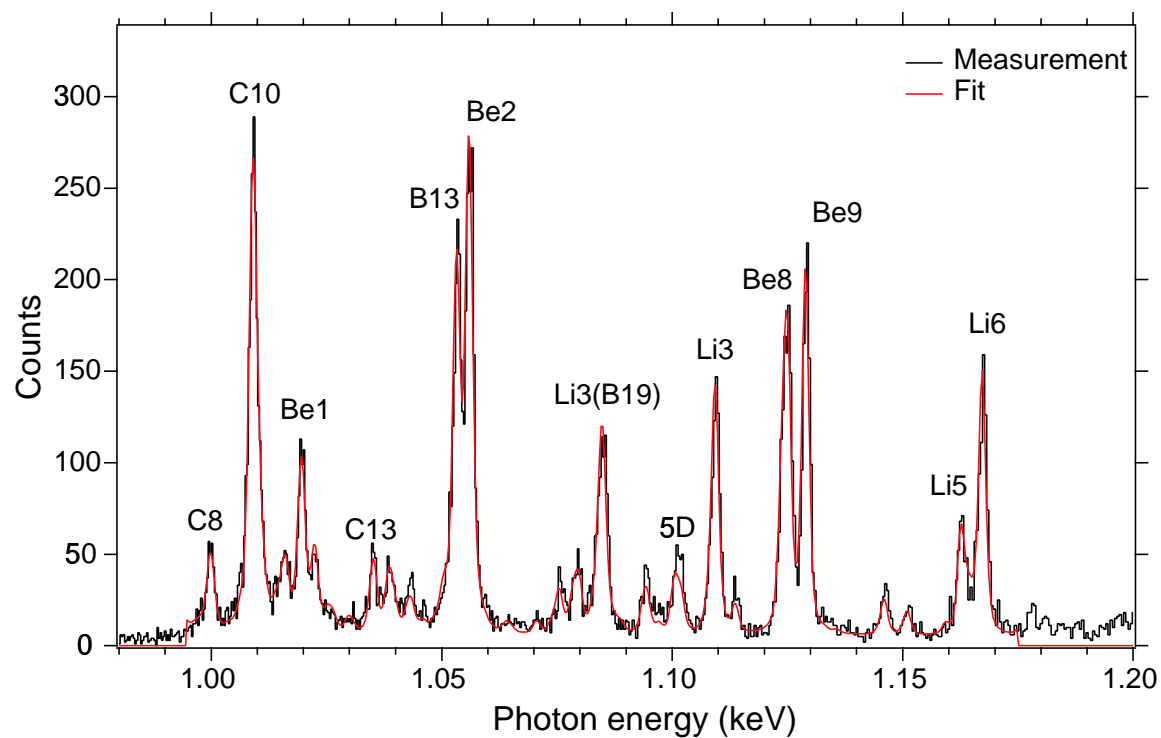


Figure 2. Crystal spectrometer spectrum of the Fe L-shell transitions at an electron beam energy of 2.93 keV. The black line is the measurement, and the red line is the fitted spectrum.

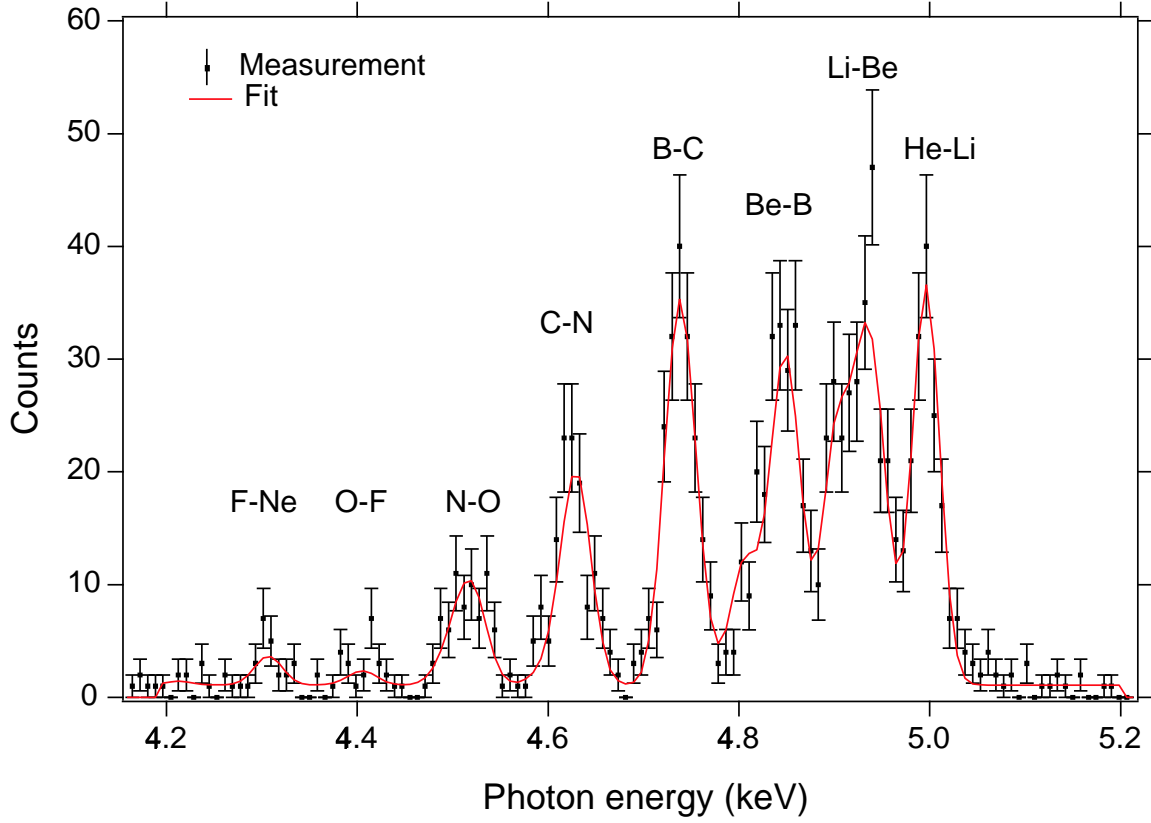


Figure 3. RR spectrum of Fe L-shell measured with the XRS (dots with statistic error bars) at a electron beam energy of 2.93 keV. The peaks are labeled in the form A-B, where A represents charge state of the ion capturing an electron and B is the charge state after recombination. For example, "B-C" denotes the photon emitted when B-like Fe^{21+} radiatively recombines to yield C-like Fe^{20+} . All capture is to the $n=2$ shell. The red line is the fit to the measurement.

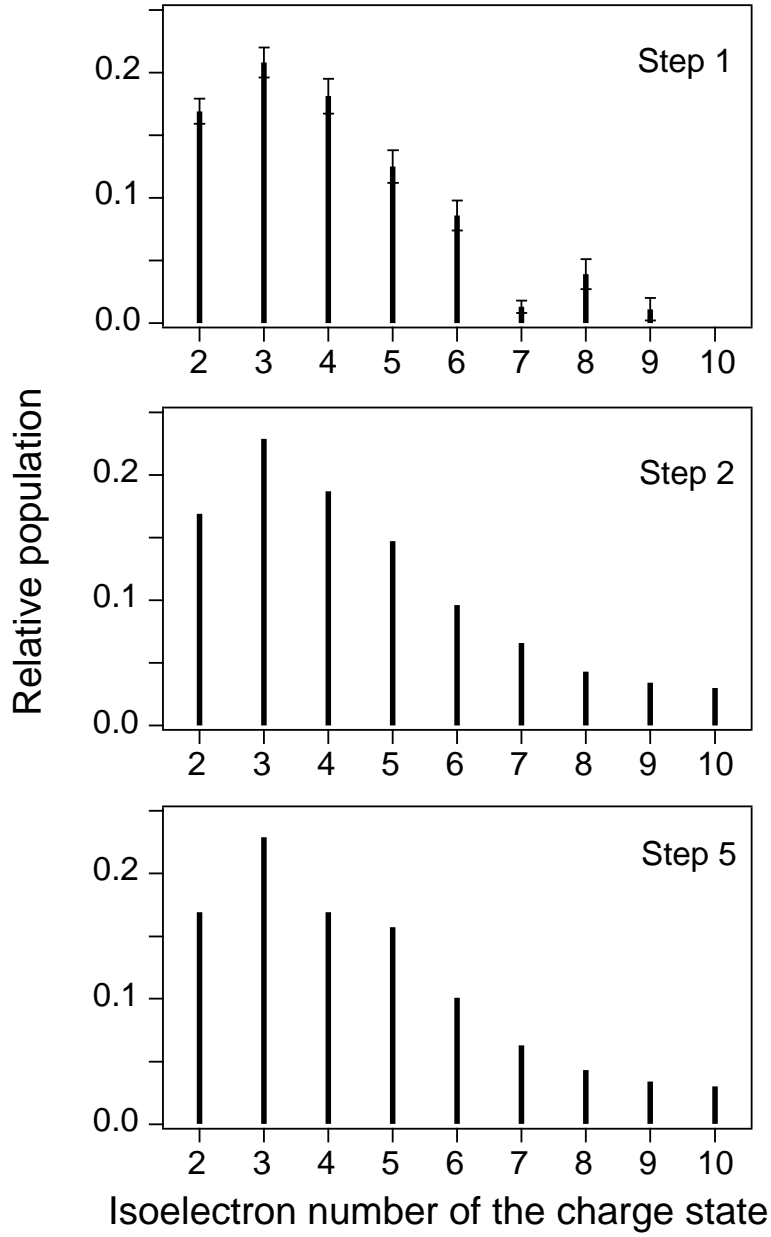


Figure 4. Charge balance derived from three different analysis steps (details see Section 3) for the spectrum taken at 2.93 keV. The charge balance in Step one (the top figure) was derived directly from the XRS measured RR using theoretical RR cross sections and relative positions of the emission. The charge balance in Step two (middle figure) was derived from the direct excitation lines measured by the XRS by fixing all theoretical excitation cross sections and polarization factors. The charge balance in Step 5 (bottom figure) was derived from the fit of XRS direct excitation lines with the theoretical cross sections adjusted to reflect the individual line ratios measured in the crystal spectrometer.

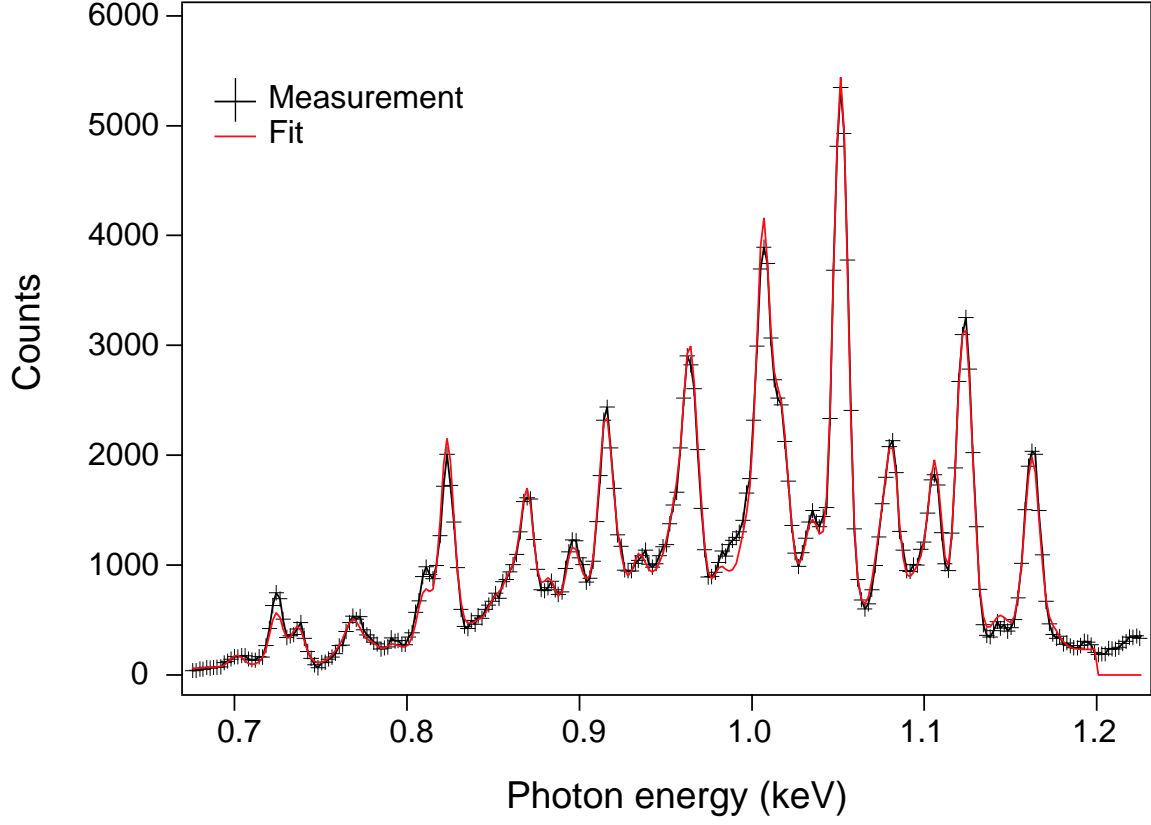


Figure 5. The XRS spectrum of the Fe L-shell emission measured (crosses) and its fit (solid line, red) in step 5 for the electron beam energy of 2.93 keV. Note that pure theoretical data was used to fit the Ne-like Fe lines. The discrepancies between measurement and fit near 730 eV and 810 eV is likely due to the theoretical cross sections of these lines (Brown et al. 2006).

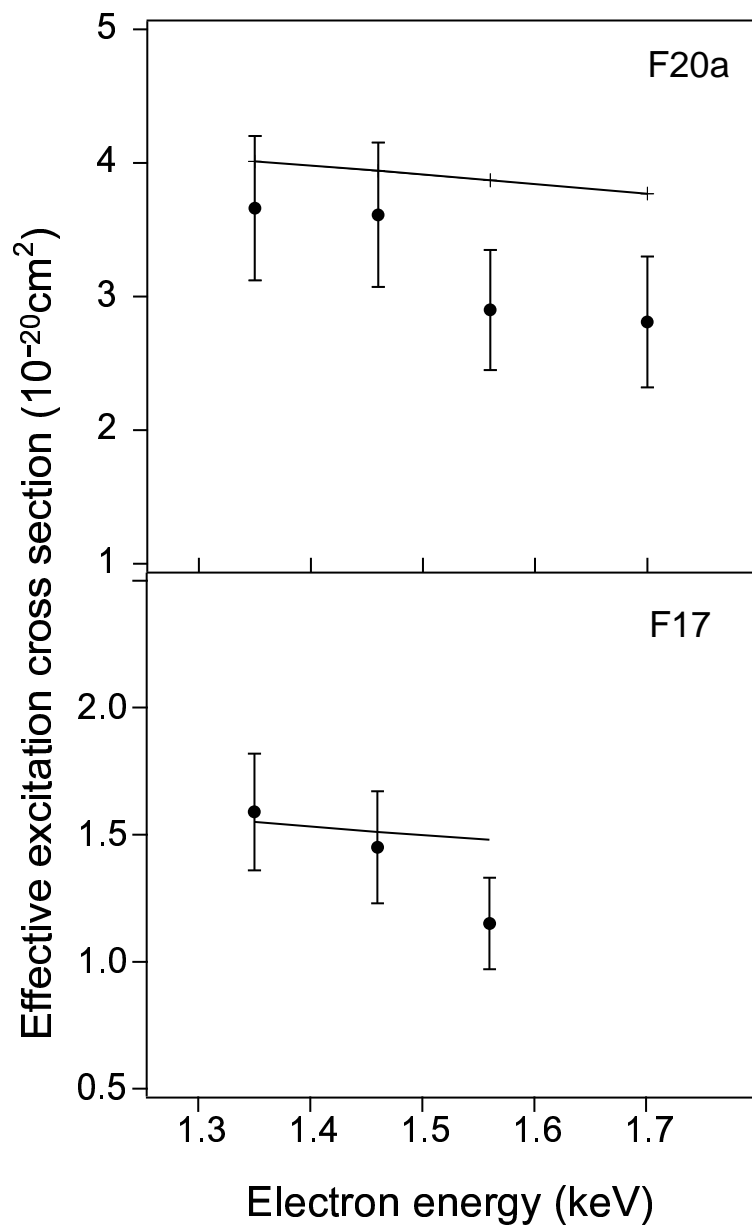


Figure 6. Selected, measured effective cross sections (dots with error bars) for two F-like Fe lines. Theoretical calculations using FAC are shown as a solid line.

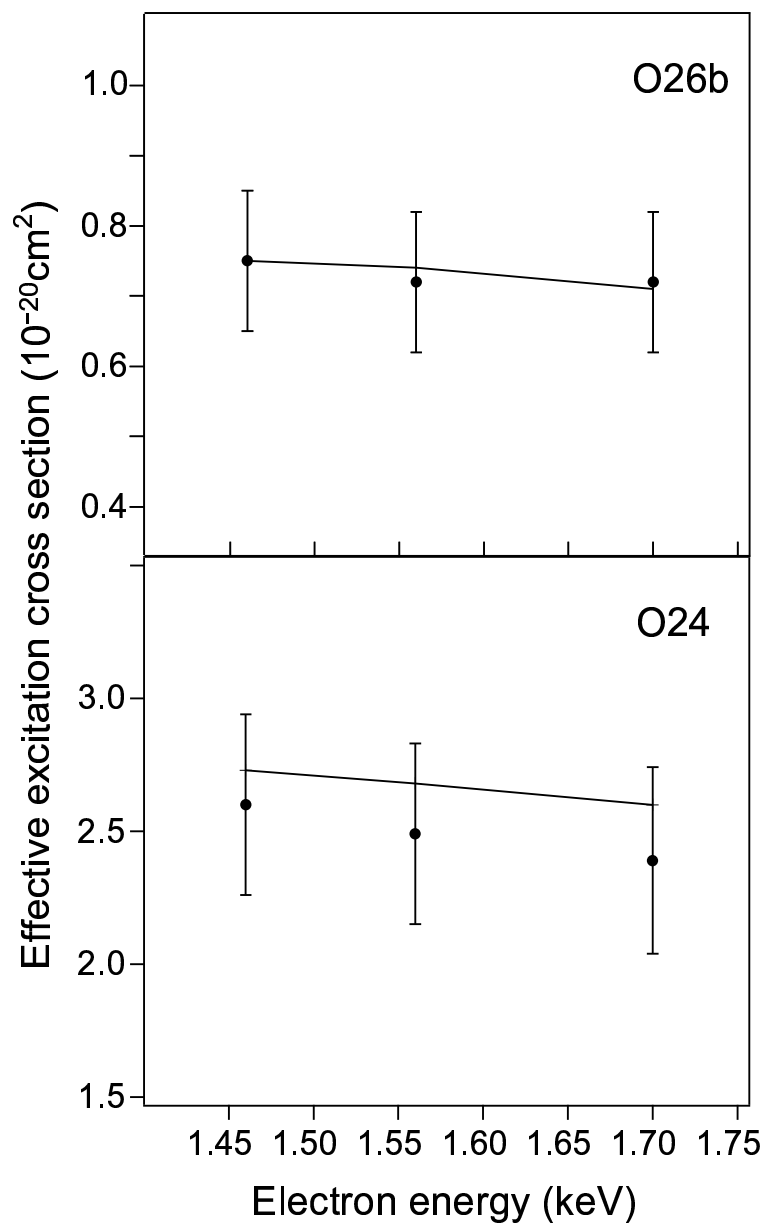


Figure 7. Measured effective cross sections (dots with error bars) for two O-like Fe lines. Theoretical calculations using FAC are shown as a solid line.

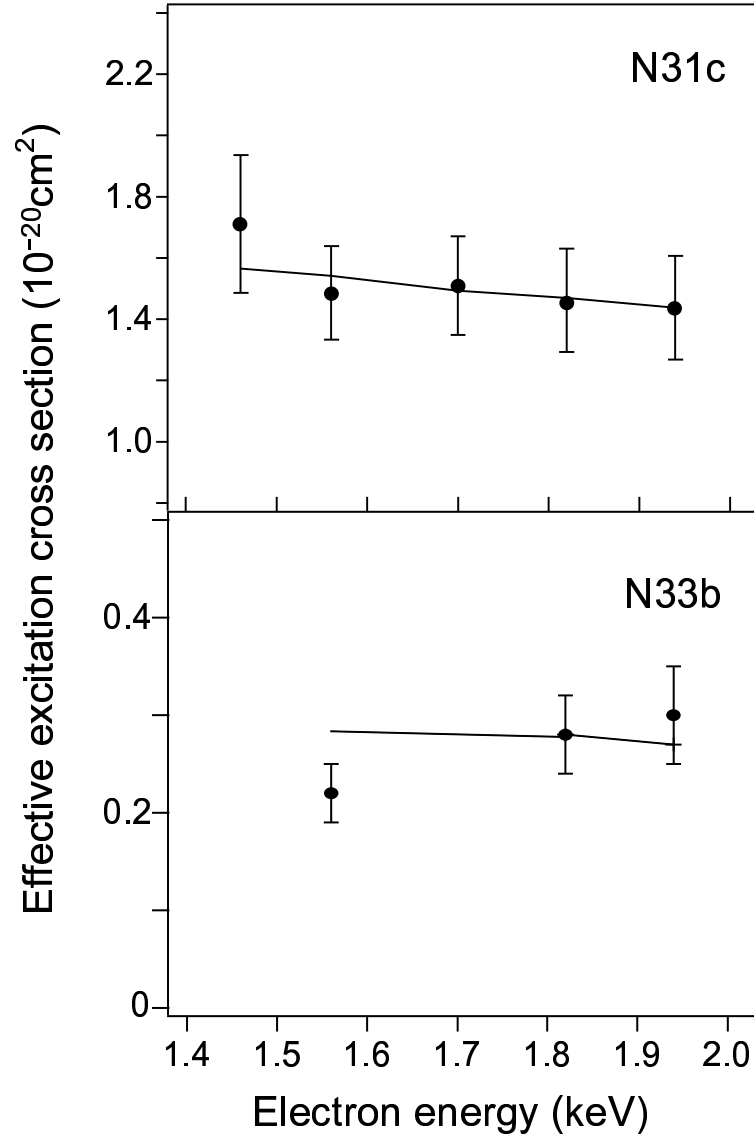


Figure 8. Measured effective cross sections (dots with error bars) for two N-like Fe lines. Theoretical calculations using FAC are shown as a solid line.

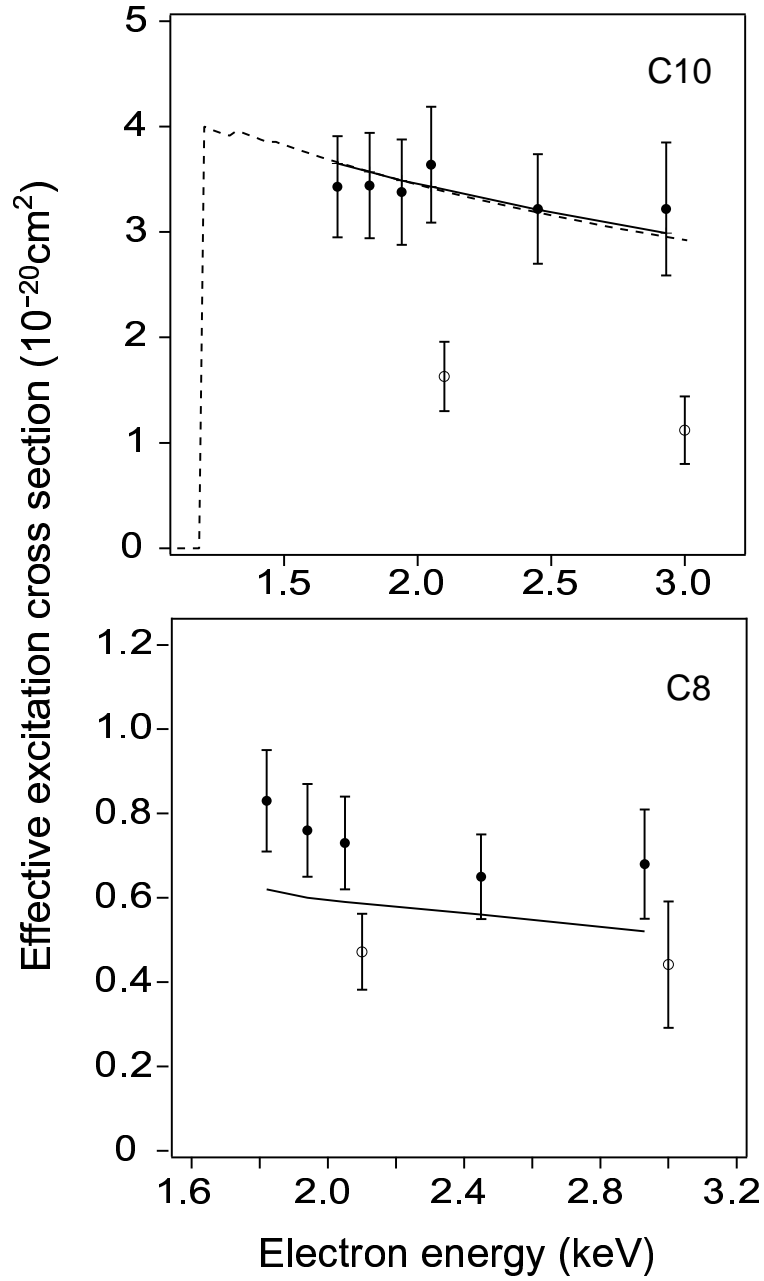


Figure 9. Measured effective cross sections (dots with error bars) for two C-like Fe lines. Theoretical calculations using HULLAC and FAC are shown as a dashed line and solid line, respectively. Also plotted are previous measurements (circles with error bars). The difference seen between the two sets of measurements for line C10 is attributed to density effects, as discussed in the text.

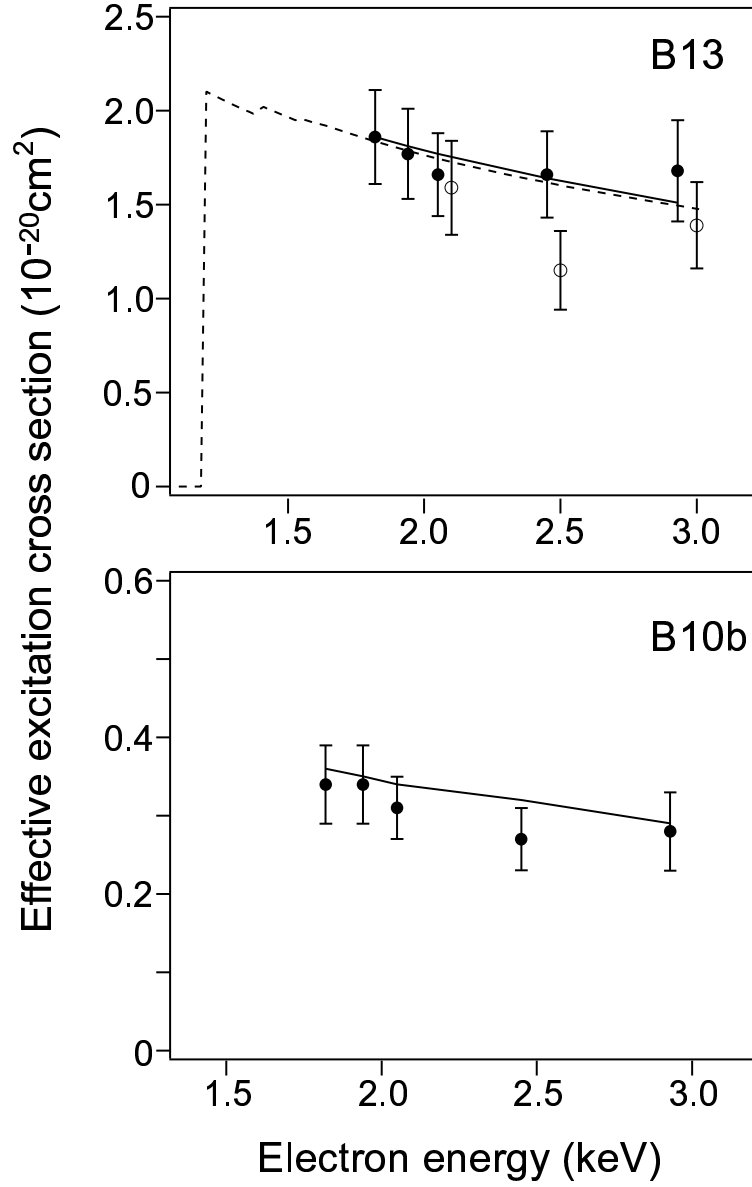


Figure 10. Measured effective cross sections (dots with error bars) for two B-like Fe lines. Theoretical calculations using HULLAC and FAC are shown as a dashed line and solid line, respectively. Also plotted are previous measurements (circles with error bars).

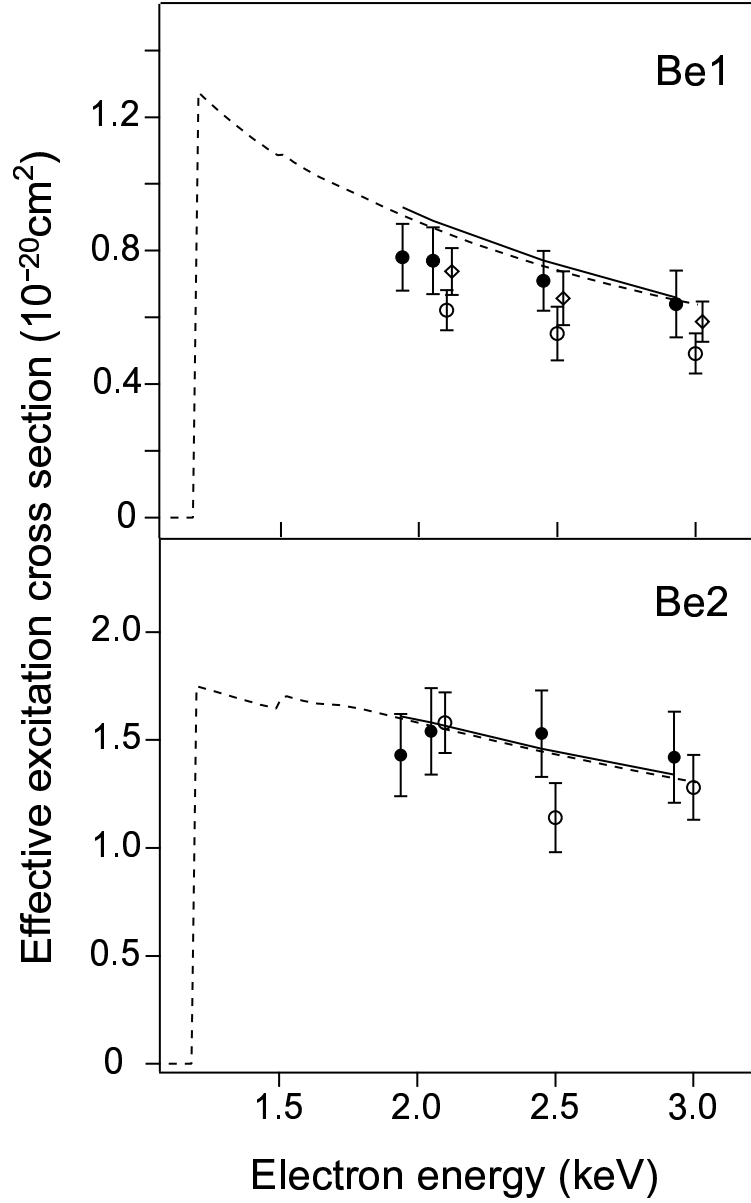


Figure 11. Measured effective cross sections (dots with error bars) for two Be-like Fe lines. Theoretical calculations using HULLAC and FAC are shown as a dashed line and solid line, respectively. Also plotted are previous measurements (circles with error bars), and the modified results (open diamonds) by reanalyzing the previous measurement accounting for the B6 line intensity (for details see Discussion section). The energy value of these data points are shifted by 20 eV to more clearly show the changes.

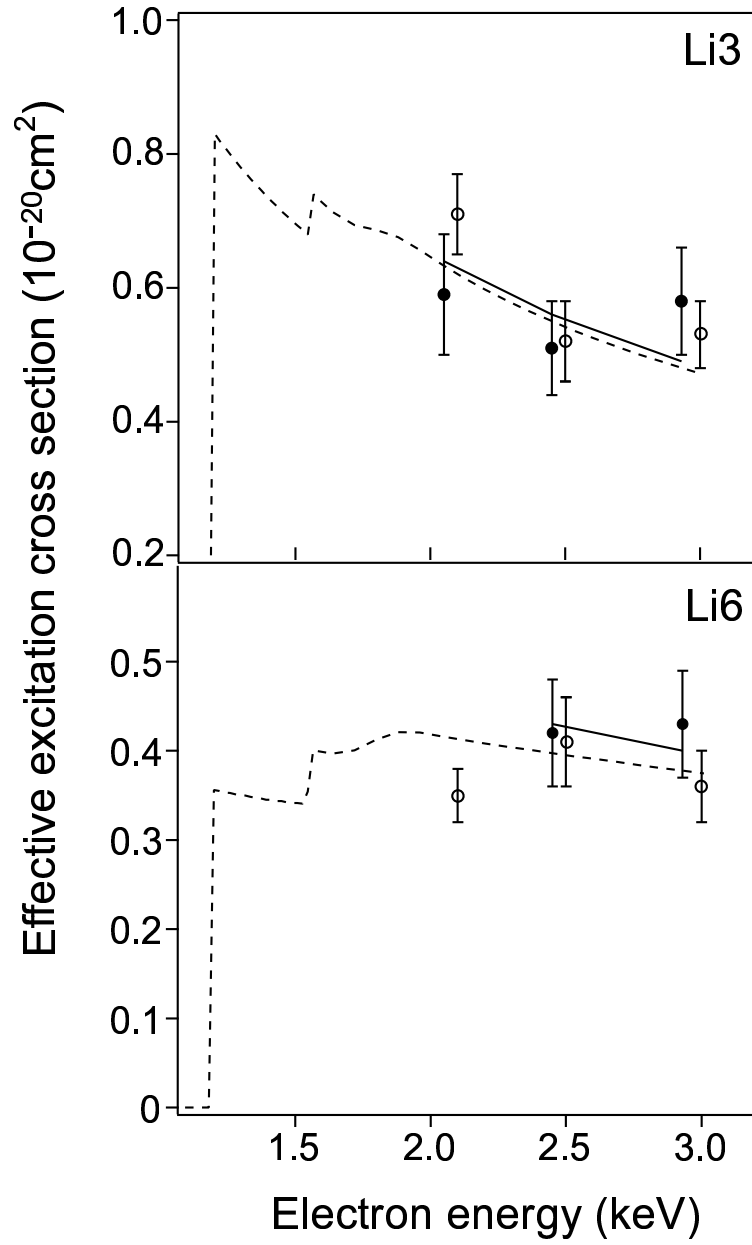


Figure 12. Measured effective cross sections (dots with error bars) for two Li-like Fe lines. Theoretical calculations using HULLAC and FAC are shown as a dashed line and solid line, respectively. Also plotted are previous measurements (circles with error bars).

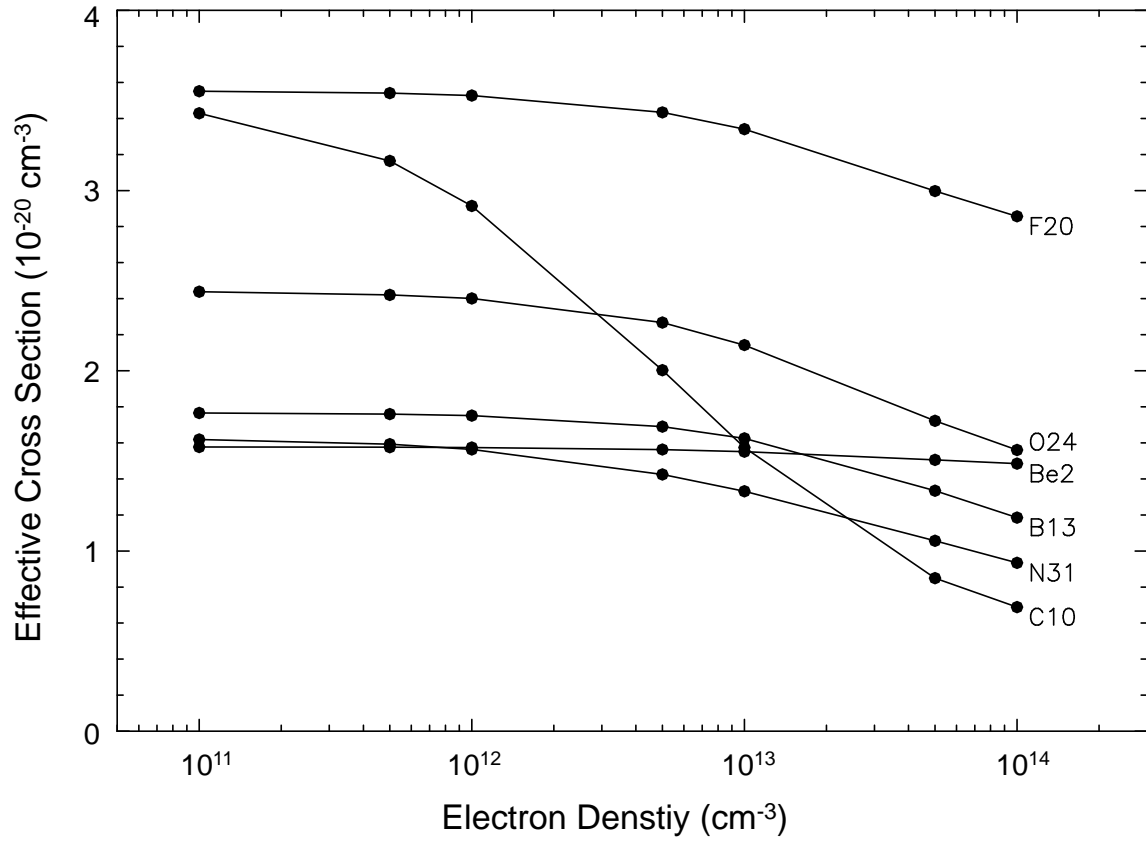


Figure 13. The effective excitation cross sections for some density sensitive Fe L-shell lines.

REFERENCES

- Audley, M. D., et al, 1999, SPIE 3765, 751
- Bar-Shalom, A., Klapisch, M., & Oreg, J. 2001, J. Quant. Spec. Radiat. Transf., 71, 169
- Behar, E., Cottam, J., & Kahn, S. M., 2001, ApJ, 548, 966
- Beiersdorfer, P., Phillips, T. W., Wong, K. L., Marrs, R. E., & Vogel, D. A., 1992, Phys. Rev. A, 46, 3812
- Beiersdorfer, P. & Wargelin, B. J., 1994, Rev. Sci. Instrum. 65, 13
- Beiersdorfer, P., et al, 1996, Phys. Rev. A. 53, 3974
- Beiersdorfer, P., et al, 1999, PRA 60, 4156
- Beiersdorfer, P., et al, 2002, ApJ 576, L169
- Beiersdorfer, P. & Fujimoto, T., 2001, Preceedings of the 3rd Plasma Polarization Spectroscopy workshop, Livermore, California, UCRL-ID-146907
- Beiersdorfer, P., 2003, Annu. Rev. Astron. Astrophys., 41, 343
- Beiersdorfer, P., et al, 2004, ApJ., 610, 616
- Boyce, K. R., et al, 1999, SPIE 3765, 741
- Brown, G. V., Beiersdorfer, P., Liedahl, D. A., Widmann, K., Kahn, S. M. & Clothiaux, E. J., 2002, ApJS, 140, 589
- Brown, G. V., Beiersdorfer, P., Chen, H., Chen, M. H. & Reed, K. J., 2001, ApJ, 557, L75
- Brown, G. V., Beiersdorfer, P., Liedahl, D. A., Widmann, K. & Kahn, S. M. 1998, ApJ, 502, 1015
- Brown, G. V., Beiersdorfer, P., & Widmann, K., 1999, Rev. Sci. Instrum. 70, 280
Appl. Phys. 49, 1019
- Brown, G. V., Beiersdorfer, P., et al., 2006, submitted to PRL.
- Chantrenne, S., Beiersdorfer, P., Cauble, R., & Schneider, M. B., 1992, Phys. Rev. Lett. 69, 265
- Chen, H., Beiersdorfer, P., Scofield, J. H., Gendreau, K. C., Boyce, K. R., Brown, G. V., Kelley, R. L., Porter, F. S., Stahle, C. K., Szymkowiak, A. E., & Kahn, S. M., 2002, ApJ 567, L169
- Chen, H., Beiersdorfer, P., Heeter, L. A., Liedahl, D. A., Naranjo-Rivera, K. L., Träbert, E., Gu, M. F. & Lepson, J. K. 2004, ApJ, 611, 598

- Chen, H., Beiersdorfer, P., Scofield, J., K. C., Boyce, K. R., Brown, G. V., Kelley, R. L., Kilbourne, C. K., Porter, F. S., Gu, M. F., & Kahn, S. M., 2002, *ApJ* 618, 1086
- Dcaux, V., Jacobs, V.L., Beiersdorfer, P., Liedahl, D.A., & Kahn, S. M., 2003, *Phys. Rev. A*, 68, 012509
- Gendreau, K. C., et al, 1999, *SPIE* 3765, 137
- Gu, M. F., Kahn, S. M., Savin, D. W., Beiersdorfer, P., Liedahl, Brown, G. V., Reed, K. J., Bhalla, C. P., & Grabbe, S. R., 1999a, *ApJ*, 518, 1002
- Gu, M. F., Savin, D. W., & Beiersdorfer, P., 1999b, *J. Phys. B*, 32, 5371
- Gu, M. F., Kahn, S. M., Savin, D. W., Bahar, E., Beiersdorfer, P., Brown, G. V., Liedahl & Reed, K., 2001, *ApJ*, 563, 462
- Gu, M. F., 2003, *ApJ*, 582, 1241
- Gu, M. F., 2005, *ApJS*, 156, 105
- Henke, B. L., Gullikson, E. M., & Davis, J. C. 1993, *At. Data Nucl. Data Tables*, 54, 181
- Kahn, S. M., & Liedahl, D. A., 1990, in *Iron Line Diagnostics in X-ray Sources*, edited by A. Treves, G. C. Perola & L. Stella, Springer-Verlag, p3
- Paerels, F. B. S. & Kahn, S. M., 2003, *Ann. Rev. Astron. Astrophys.*, 41, 291
- Phillips, K. J. H., Bhatia, A. K., Mason, H. E., & Zarro, D. M., 1996, *ApJ*, 466, 549
- Kelley, R. L., et al, 1999, *SPIE*, 3765, 114
- Levine, M. A., Marrs, R. E., Henderson, J. R., Knapp, D. A., & Schneider, M. B., 1988, *Physics Scripta*, T22, 157
- Ogawara, Y. 1998, *Proc. of IAU Symp. No. 188 Kyoto*
- Porter, F. S., et al, 1999, *SPIE* 3765, 729
- Porter, F. S., et al, 2000, *SPIE* 4140, 407
- Saloman, E. B., Hubbell, J. H., & Scofield, J. H., 1988 *At. Data Nucl. Data Tables* 38, 1
- Scofield, J. H. 1989, *Phys. Rev. A*, 40, 3054
- Scofield, J. H. 1991, *Phys. Rev. A*, 44, 139
- Smith, R. K., Brickhouse, N. S., Liedahl, D. A., & Raymond, J. C., 2001, *ApJ*, 556, L91
- Stahle, C. K., et al, 1999, *SPIE* 3765, 82

- Utter, S. B., Beiersdorfer, P., Crespo Lopez-Urrutia, J. R., & Widmann, K., 1999, Nuclear Instrum. and Methods in Physics Research: Section A 428, 276
- Wargelin, B. J., Beiersdorfer, P., Liedahl, D. A., Kahn, S. M., & von Goeler, S., 1998, ApJ496, 1031
- Xu, H., Kahn, S. M., Peterson, J. R., et al., 2002, ApJ579, 600
- Zhang, H. L. & Sampson, D. H., 1989, Atomic Data and Nuclear Data Tables, 43, 1
- Zhang, H. L., Sampson, D. H., & Clark, R. E. H., 1990, Phys. Rev. A, 41,198